

AD-A051 122

AIR FORCE GEOPHYSICS LAB HANSCOM AFB MASS
LARGE SCALE OPTICAL MAPPING OF THE IONOSPHERE. (U)
OCT 77 E J WEBER, J W LLOYD, J BUCHAU
AFGL-TR-77-0236

F/G 4/1

UNCLASSIFIED

NL

| OF |

AD
A051122



AD A051122

AFGL-TR-77-0236
ENVIRONMENTAL RESEARCH PAPERS, NO. 611



2
B.S.

Large Scale Optical Mapping of the Ionosphere

E. J. WEBER, Capt, USAF
J. BUCHAU
R. H. EATHER
J. W. F. LLOYD

AD No. —
DDC FILE COPY

21 October 1977

DDC
RECEIVED
MAR 13 1978
B

Approved for public release; distribution unlimited.

This research was supported by the Air Force In-House Laboratory Independent Research Fund.

SPACE PHYSICS DIVISION PROJECT ILIR
AIR FORCE GEOPHYSICS LABORATORY
HANSCOM AFB, MASSACHUSETTS 01731

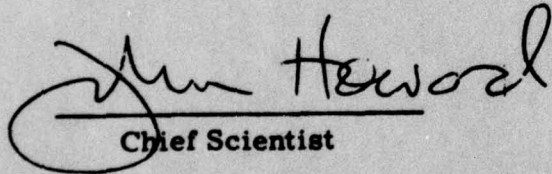
AIR FORCE SYSTEMS COMMAND, USAF



This report has been reviewed by the ESD Information Office (OI) and is releasable to the National Technical Information Service (NTIS).

This technical report has been reviewed and is approved for publication.

FOR THE COMMANDER


Chief Scientist

Qualified requestors may obtain additional copies from the Defense Documentation Center. All others should apply to the National Technical Information Service.

⑨ Environmental research papers

Unclassified

SECURITY CLASSIFICATION OF THIS PAGE (When Data Entered)

REPORT DOCUMENTATION PAGE		READ INSTRUCTIONS BEFORE COMPLETING FORM	
1. REPORT NUMBER AFGL-TR-77-0236, AFGL-ERP-611	2. GOVT ACCESSION NO.	3. RECIPIENT'S CATALOG NUMBER	
4. TITLE (and Subtitle) LARGE SCALE OPTICAL MAPPING OF THE IONOSPHERE	5. TYPE OF REPORT & PERIOD COVERED		
6. AUTHOR(S) E. J. Weber, [redacted] J. W. F. Lloyd J. Buchau R. H. Eather	6. PERFORMING ORG. REPORT NUMBER ERP No. 611		
7. PERFORMING ORGANIZATION NAME AND ADDRESS Air Force Geophysics Laboratory (PHI) Hanscom AFB Massachusetts 01731	8. CONTRACT OR GRANT NUMBER(s)		
10. PROGRAM ELEMENT, PROJECT, TASK AREA & WORK UNIT NUMBERS 61101F HIR6A01	11. REPORT DATE 21 Oct 77		
11. CONTROLLING OFFICE NAME AND ADDRESS Air Force Geophysics Laboratory (PHI) Hanscom AFB Massachusetts 01731	12. NUMBER OF PAGES 31		
14. MONITORING AGENCY NAME & ADDRESS (if different from Controlling Office)	15. SECURITY CLASS. (of this report) Unclassified		
16. DISTRIBUTION STATEMENT (of this Report) Approved for public release; distribution unlimited.	15a. DECLASSIFICATION/DOWNGRADING SCHEDULE		
17. DISTRIBUTION STATEMENT (of the abstract entered in Block 20, if different from Report)	DDC REFINED MAR 13 1978 REGISTERED B		
18. SUPPLEMENTARY NOTES *KEO Consultants, 26 Prentice Road, Newton, MA 02159, and Department of Physics, Boston College, Chestnut Hill, MA 02167. This research was supported by the Air Force In-House Laboratory Independent Research Fund.			
19. KEY WORDS (Continue on reverse side if necessary and identify by block number) All sky imaging photometer Equatorial airglow Scintillations Dayside auroras			
20. ABSTRACT (Continue on reverse side if necessary and identify by block number) A new instrument for all sky, spectrophotometric imaging of aurora and airglow has been installed in the Air Force Geophysics Laboratory's Airborne Ionospheric Observatory. Initial observations of equatorial and near-equatorial 6300/401 airglow show the existence of north-south aligned regions of airglow depletion. These dark bands often extend more than 1200 km in the north-south direction and 50 to 200 km in the east-west direction. Simultaneous airborne ionospheric soundings indicate that these regions of airglow depletion	→ next page		

DD FORM 1 JAN 73 1473 EDITION OF 1 NOV 65 IS OBSOLETE

Unclassified

SECURITY CLASSIFICATION OF THIS PAGE (When Data Entered)

1
409 578
Hew

Unclassified

SECURITY CLASSIFICATION OF THIS PAGE(When Data Entered)

20. Abstract (Continued)

cont. → are characterized by an increase in the virtual height of the F-layer. A simple model of field aligned electron density depletion in the bottomside of the F-layer explains both the airglow observations and the ionospheric soundings. Initial auroral zone measurements show the structure and dynamics of the subvisual auroras in the noon sector that result from dayside precipitation. UHF satellite-to-aircraft propagation through the F-region auroras result in amplitude scintillations, both in the noon and midnight local time sectors. ↗

Unclassified

SECURITY CLASSIFICATION OF THIS PAGE(When Data Entered)

Preface

The authors wish to thank J. G. Moore for providing the airborne spectrometer measurements; MSgt George Coolidge, A1C Paul Diroll, and A1C Charles Theisen for reduction and presentation of the all sky photometer images; and J. P. McClure and A. L. Snyder for helpful comments in the preparation of this paper.

The success of these airborne expeditions was due to the efforts of Major Calvin Smith and other members of the 4950th Test Wing, Wright-Patterson AFB, Ohio.

This research was supported by the Air Force In-House Laboratory Independent Research Fund of the Air Force Geophysics Laboratory, Air Force Systems Command.

ACCESSION for		
NTIS	White Section	<input checked="" type="checkbox"/>
DDC	Buff Section	<input type="checkbox"/>
UNANNOUNCED		<input type="checkbox"/>
JUSTIFICATION _____		
BY _____		
DISTRIBUTION/AVAILABILITY CODES		
Dist.	AVAIL.	and/or SPECIAL
A		

Contents

1. INTRODUCTION	7
2. ALL-SKY IMAGING PHOTOMETER	8
3. EQUATORIAL AIRGLOW	12
3.1 Introduction	12
3.2 Equatorial Airglow Structures	12
3.3 Observations	13
3.4 Drifts	15
3.5 Ionosphere Measurements	16
3.6 VHF Amplitude Scintillations	20
3.7 Summary of Equatorial Measurements	20
4. ARCTIC MEASUREMENTS	22
4.1 Introduction	22
4.2 Observations	23
5. SUMMARY AND DISCUSSION	28
REFERENCES	31

Illustrations

1. All-Sky Imaging Photometer Optics Schematic	9
2. All-Sky Imaging Photometer System Block Diagram	10
3. All Sky (155° field of view) 6300 Å OI Airglow Images at 15-Minute Intervals, From 0100 UT to 0545 UT, 17 March 1977	14

Illustrations

4. The C. G. Longitude of the Eastern and Western Edges of the Airglow Depletion Shown in Figure 1	16
5. Virtual Height/Range Plot of Ionosonde Returns Associated With the 6300 Å Airglow Depletion	17
6. Model of an Eastward Drifting, Bottomside Ne Depletion or Corrugation Based on Observed Ionosonde and Airglow Parameters	18
7. VHF Amplitude Scintillation Index Associated With the Passage of the Ionization Depletion Through the Satellite-to-Aircraft Ray Path	21
8. C. G. Latitude/Local Time Plot of the Flight Track of 21 January 1977	24
9a. 6300 Å (top) and 4278 Å (bottom) Images for the Flight of 21 January 1977 From 0210 UT to 0550 UT at 10-Minute Intervals	25
9b. 6300 Å (top) and 4278 Å (bottom) Images for the Flight of 21 January 1977 From 0600 UT to 0950 UT at 10-Minute Intervals	26
10. C. G. Latitude/Local Time Plot of Subsatellite Track for Two DNA WIDEBAND Satellite Orbits	27

Table

1. Summary of System Specifications	11
-------------------------------------	----

Large Scale Optical Mapping of the Ionosphere

1. INTRODUCTION

A program for large-scale, optical mapping of the ionosphere was undertaken to more effectively monitor ionospheric features through remote sensing of associated auroral and airglow spectral emissions. Previous techniques in this area were limited by the inability to combine adequate spatial, temporal, and spectral resolution with sufficient sensitivity to measure low-intensity emissions. These emissions reflect such important aspects of ionospheric processes as flux, type, and average energy of particles precipitating into the upper atmosphere, as well as non-particle produced irregularities in the equatorial F-region.

To conduct this program, a new instrument for monochromatic, all sky observations of aurora and airglow was developed and has recently been installed in the Air Force Geophysics Laboratory's Airborne Ionospheric Observatory, a KC-135 aircraft instrumented for ionospheric research. The imaging system incorporates the necessary spectral, temporal, and spatial resolution to provide a unique diagnostic tool for the study of aurora and airglow.

To monitor appropriate ionospheric energy input parameters, four relevant wavebands are used. The total energy flux of precipitating particles is monitored by recording the 4278 N_2^+ emission band, which is also proportional to the height-integrated ionization rate. The 6300 OI atomic oxygen emission is used to obtain

(Received for publication 17 October 1977)

the fraction of the total input energy deposited at F-layer height. Considerable energy is deposited and ionization generated by proton precipitation, which is monitored by observation of the 4861 H_{β} (Hydrogen Balmer) emission. For observations of equatorial F-region irregularities, measurements are made of the 6300 Å and 5577 Å OI airglow. Intensity variations in these emissions are combined with radiowave measurements to infer dynamics in the F-region plasma.

A brief description of the all-sky imaging photometer as well as initial results from experiments conducted at the magnetic equator and in the auroral zones are presented in this report.

2. ALL-SKY IMAGING PHOTOMETER

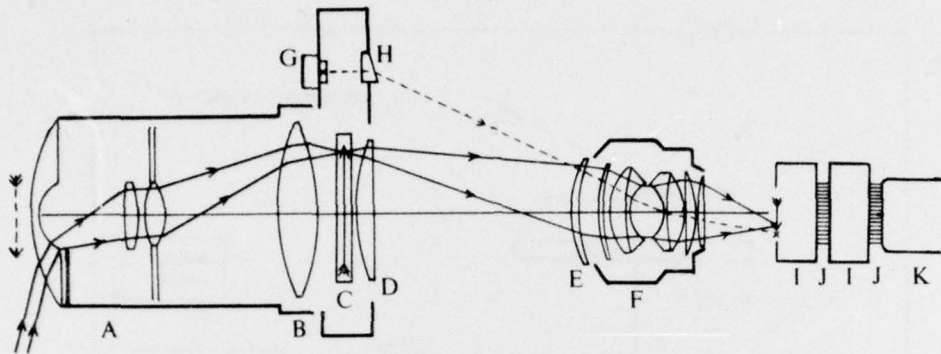
An all-sky imaging system similar to one for ground-based observations¹ was developed for airborne operation. The optics (Figure 1) employ a 155° field of view and are telecentric in design, ensuring the same size light cone at the focal plane for each point in the field of view, thus allowing narrowband interference filters to be used. At full aperture of f1.4, 25 Å filters can be used. Four such filters mounted on a filter wheel allow sequential measurements for the most important auroral and airglow emissions.

The auroral/airglow field is then re-imaged onto the faceplate of a two-stage image intensifier that is fiber-optically coupled to a LLL SEC TV tube. This is a charge-integrating tube that allows for time exposures of up to 3 sec at room temperature.

Sequential pictures at different wavelengths are recorded on a time-lapse video tape recorder (see system block diagram in Figure 2) and temporarily stored on a multi-track video disc that is used to drive four black and white TV monitors that continuously display the last picture taken through each filter. These pictures are continually updated as the filter wheel rotates through the four-filter sequence.

For very-low-level emissions such as H_{β} , the nonspectral background emissions form a significant part of the total signal and must be subtracted to obtain the true H_{β} emission. To achieve this, the picture at the H_{β} wavelength is temporarily stored on one of the video disc tracks and a second picture is taken through a background filter centered some 30 Å below the H_{β} wavelength. The second picture is subtracted from the first, using the A minus B option on the TV monitor, and the resultant H_{β} picture is recorded and displayed.

1. Mende, S. B., and Eather, R. H. (1976) Monochromatic all sky observations and auroral precipitation patterns, J. Geophys. Res. 81:3771.



- A All Sky Lens (155°)
- B 3" F.L. Auxiliary Lens (Bi-Convex)
- C Narrow Band Interference Filter
- D 7" F.L. Lens (Plano-Convex)
- E 3 Diopter Close Up Lens (Meniscus)
- F Nikon 55mm/F1.2 Lens
- G Carbon 14 Radioactive Light Source
- H Wedge Prism (10 deg.)
- I Varo Image Intensifier (Low EBI)
- J Fibre Optics Coupling
- K Westinghouse LLL SEC TV Tube

Figure 1. All-Sky Imaging Photometer Optics Schematic

To display the average energy of the electrons generating various auroral features in the field of view, a RGB color TV monitor is used. Since the average electron energy is characterized by the $6300 \text{ \AA} \text{ OI}/4278 \text{ \AA} \text{ N}_2^+$ ratio, the $4278 \text{ \AA} \text{ N}_2^+$ picture is used to drive the blue gun of the monitor and the $6300 \text{ \AA} \text{ OI}$ picture to drive the red gun, thereby producing a color characteristic of the electron energy.

An absolute intensity reference is supplied by a C^{14} radioactive light source that is imaged on the corner of each frame. Date, time, and filtering information is binary encoded on each picture, and date and time are also presented numerically on each picture. In addition to video recording, the TV monitors are photographed each cycle by a 16-mm, time-lapse camera.

The time and control sequencing for the instrument is provided by a fully programmable, special-purpose sequencer that controls the mechanical operation, exposure time, high voltage appropriate for each filter, distribution of video signals to appropriate discs, and camera exposure. Preprogrammed exposure sequences allow rapid change of operational modes appropriate to changing auroral conditions.

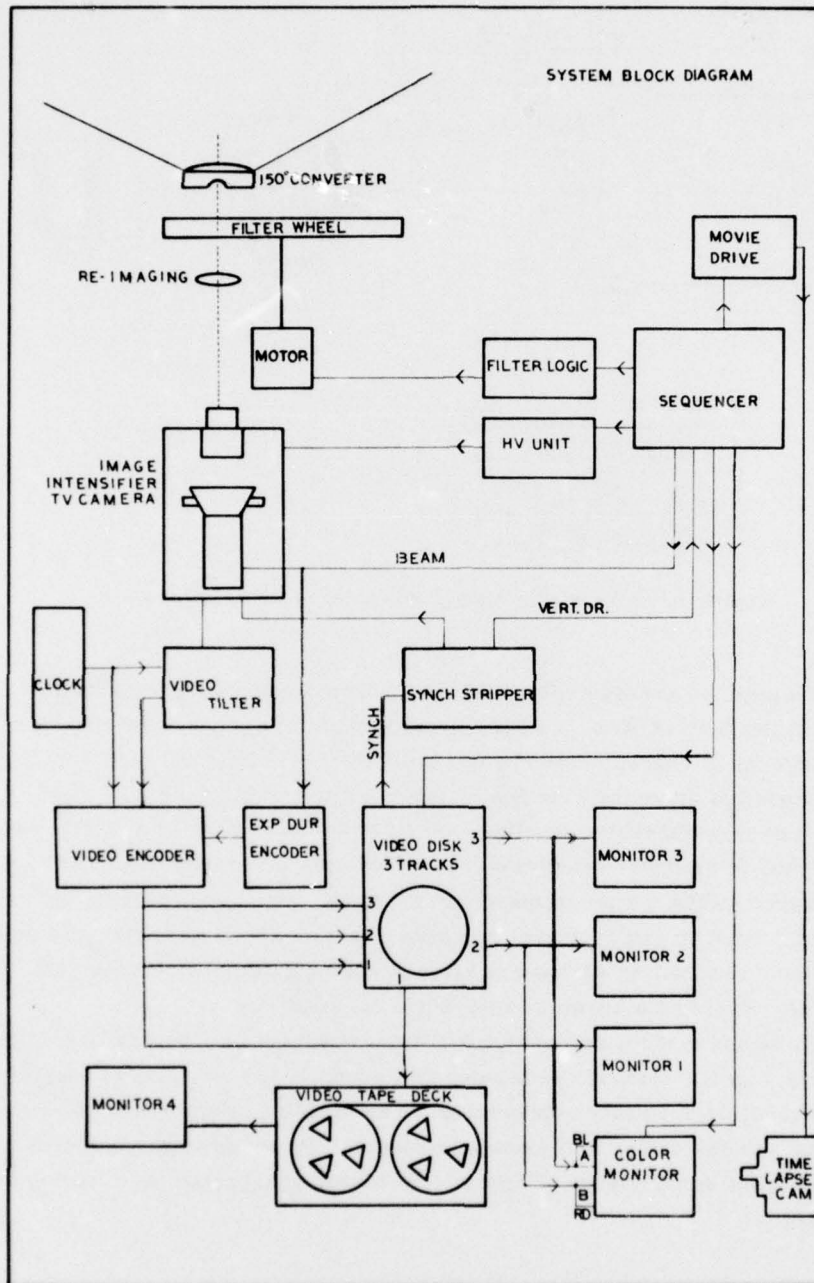


Figure 2. All-Sky Imaging Photometer System Block Diagram

Certain modifications have been made to the disc for aircraft use, to ensure proper operation and to prevent possible damage at take off or landing. The complete instrument has been shock mounted, and the heads have automatic lifters that remove the heads from the disc for take off and landing.

A summary of system operational parameters is given in Table 1.

Table 1. Summary of System Specifications

Field of View:	155°
Pass Band:	25 Å at f 1.4; 5 Å at f 8
Resolution:	1/2° zenith, 2° horizon
Spectral Response:	S - 20, exceeding 100 μA/lumen
Picture Storage:	No detectable degradation for up to 3 sec
Tube Gain:	Photon noise granularity visible above tube noise
Threshold Sensitivity:	20 R at 2 sec exposure 1 kR at 30 frames/sec
Dynamic Range:	20 R to 10 kR covered by 3 preset HV settings
Flatness of Field:	30 percent loss at edge of field
Repetition Rate:	Typically 20 sec for complete filter cycle
Temporary Storage:	Video disc, three video tracks + one sync track
Permanent Storage:	Video tape deck, time-lapse type (9 hr recording time on a single reel): 16 mm color movie camera
Process Controller:	In-field programming capability
Display Systems:	Four black and white monitors, 9 in. diagonal; Color monitor, RGB and A-B input, 12 in. diagonal
Real-Time Display:	Simultaneous fully registered display of three filter channels. Capability of displaying difference of any two pictures. Display of two or three filters as pseudo-color on RGB monitor
Character Generators:	Date/time display on each frame for frame identification
Digital Encoding:	Digital encoding of time and housekeeping data for computer-controlled data handling
Flight Heading:	Digital display of flight heading for recording (three digit BCD TTL compatible)

3. EQUATORIAL AIRGLOW

3.1 Introduction

A series of seven flights was conducted along the west coast of South America in March 1977 to investigate the spatial and temporal characteristics of large scale, F-region irregularities in the vicinity of the magnetic equator. The primary purpose of this expedition was to relate specific dynamical features of the equatorial ionosphere to the occurrence of signal fluctuations (scintillations) on satellite-to-aircraft and satellite-to-ground VHF/UHF radio transmissions. Optical imaging measurements were performed to identify the large scale, airglow structures that are associated with the F-region ionospheric irregularities. Simple modeling shows that the existence of a bottomside ionization depletion collocated with the moving band of airglow depletion can explain the observed ionogram signatures.

3.2 Equatorial Airglow Structures

Departures from spatially uniform airglow emission occur as regular features of the equatorial and near equatorial ionosphere. The prominent intertropical arcs^{2,3} appear as two bands of enhanced 6300 Å OI that reach maximum intensity at $\pm 12^\circ$ magnetic latitude and display symmetry with respect to the dip equator. These bands coincide closely in position with the Appleton anomaly region of enhanced F-region electron density. A summary of intertropical arc morphology is presented by Weill⁴ and Kulkarni.⁵ Smaller scale airglow structures have also been investigated. Steiger⁶ presented photometric sky maps of 6300 Å and 5577 Å airglow structure from Haleakala Observatory, Hawaii. These show the existence of localized (~ 500 km diam) enhancements in 6300 Å intensity, primarily to the south of the observing station. Less frequently, highly structured north-south aligned ridges or fingers of enhanced 6300 Å emission have been observed. The 6300 Å enhancements are frequently accompanied by similar variations in 5577 Å.

-
2. Barbier, D. (1961) Less variations d'intensite la raie 6300 Å la luminescence nocturne, *Ann. Geophys.* 17:5.
 3. Barbier, D., Weill, G., and Glaume, J. (1961) L'emission de la raie rouge du ciel nocturne en Afrique, *Ann. Geophys.* 17:305.
 4. Weill, G.M. (1967) Airglow observations near the equator, in *Aurora and Airglow*, B.M. McCormac, ed., Reinhold Publ. Co., p 407.
 5. Kulkarni, P.V. (1974) Tropical airglow, *Ann. Geophys.* 30:105.
 6. Steiger, W.R. (1967) Low latitude observations of airglow, in *Aurora and Airglow*, B.M. McCormac, ed., Reinhold Publ. Co., p. 419.

Van Zandt and Peterson⁷ have shown that tropical airglow structures at 6300 Å and 5577 Å can take a variety of forms – from east-west aligned bands or arcs to narrow north-south ridges of alternately enhanced and diminished intensity, arranged along an east-west band. Eastward drift velocities on the order of a few hundred km/hr have been reported for some of these airglow irregularities. The ridges shown by Van Zandt and Peterson are typically inclined to the west of magnetic north, and are not aligned along magnetic field lines.

From simultaneous ionosonde measurements, both Van Zandt and Peterson⁷ and Steiger⁶ conclude that spatial variations in 6300 Å OI intensity result primarily from variations in the height of the F-region, rather than from changes in the electron number density at peak of the F-layer. The gradients in 6300 Å intensity along the east-west direction appear, then, to be the result of corrugations in the bottomside of the F2 layer.

3.3 Observations

All-sky (155° field of view) images of the equatorial airglow were made through 6300 Å and 5577 Å narrow band (~30 Å) interference filters, using alternate 2.5 sec exposures to produce an image at each wavelength every 30 sec. The resulting TV frames were recorded on video tape and also by photographing the TV monitors.

Figure 3 presents a series of 6300 Å images (photographs of the tape recorded video frames) obtained at 15-min intervals between 0100 and 0545 UT during a flight on 17 March 1977. The superposed grid indicates the projection of corrected geomagnetic (C.G.) longitudes (or magnetic meridians) at 1-deg intervals, for an assumed emission height of 250 km. The flight track for 17 March 1977 was a series of north-south legs (from 3° C.G. north to 3° C.G. south) along a magnetic meridian 3° west of Lima, Peru. All images have been reoriented with magnetic north on top, as shown in Figure 1. (The reversal of east and west is a result of the display scheme used.)

Care must be exercised in the interpretation of features near the edge of the field of view. Although the van Rhijn effect tends to increase the apparent airglow intensity at large zenith angles (a factor of 2.7 for 75° zenith angle at 250 km emission height), the wide angle lens suffers serious vignetting toward the edge of the field of view (a factor of 3.3, Mende et al.⁸) The two effects act in opposition, but vignetting exceeds van Rhijn enhancement at the edges, often resulting in a

7. Van Zandt, T.E., and Peterson, V.L. (1968) Detailed maps of tropical 6300 Å nightglow enhancements and their implications on the ionospheric F2 layer, *Ann. Geophys.* 24:747.
8. Mende, S.B., Eather, R.H., and Aamodt, E.K. (1977) Instrument for the Monochromatic observation of all sky auroral images, *Appl. Opt.* 16:1691.

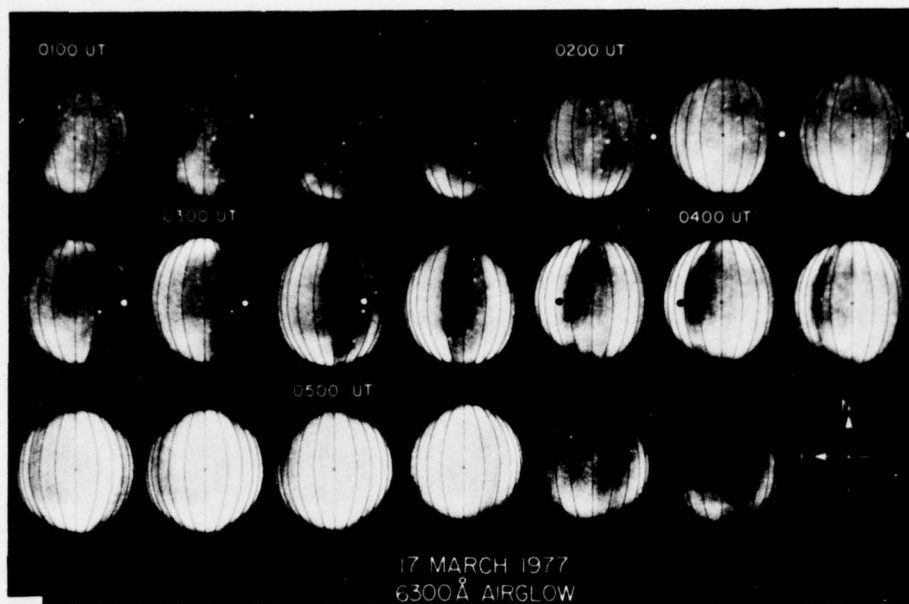


Figure 3. All Sky (155° field of view) 6300 \AA OI Airglow Images at 15-Minute Intervals, From 0100 UT to 0545 UT, 17 March 1977. The superposed grid indicates the projection of corrected geomagnetic (C.G.) longitudes, at 1 degree intervals, for an assumed emission height of 250 km. The black and white dots represent, respectively, the location of approaching and receding oblique F-region ionosonde backscatter returns

perceptible dark band around the image for the weak airglow features under consideration. The narrow N-S striations about one-half degree from zenith that can be seen in most images are the ionosonde antennas that stretch above the all-sky lens. They appear east or west of zenith, depending on whether the plane is flying north or south.

The images between 0100 UT and 0200 UT show a low level, unstructured glow ($\sim 60 \text{ R}$) with some enhancement towards the south, probably enhanced emission from the maximum of the Appleton anomaly. The Milky Way is visible in the 0100 to 0145 UT images as a slight enhancement aligned in the SE-NW direction. The 0215 UT image shows a prominent depletion in the 6300 \AA airglow in the form of a dark band that extends from south to north along much of the western horizon. The formation of this dark band can be seen as early as 0200 UT. Within the next 2.5 hr, this band travels across the sky, leaving the instrumental field of view on the eastern horizon by approximately 0445 UT. Generally, the images show that the eastern or leading edge of the airglow depletion is closely aligned in the magnetic north/south direction (best seen in the 0330 UT image). However, inspection

of selected images suggests the possibility of a 5° skew (best seen in the 0345 UT image), with the southern end of the edge leading the northern end. A detailed analysis involving the measurement of selected stars is required to eliminate experimental causes (such as small aircraft heading errors) before the precise alignment can be measured. The leading edge displays a sharp intensity gradient in the east-west direction.

From absolute airglow intensities, independently measured on the aircraft by a vertically directed, 1 meter Ebert-Fastie scanning spectrometer, a decrease from 75 R to 15 R within 100 km has been determined (J. G. Moore, private communication 1977). The western edge of the depletion region shows a somewhat more gradual, structured transition to the adjacent bright airglow region. The width of the depletion when directly overhead at 0330 UT is approximately 150 to 200 km. When the region is off-zenith, perspective effects must be considered. It is clear the region was wider before 0330 UT, but the apparent narrowing after 0330 UT could be due to perspective. The apparent width of the measured depletion region also depends on the detectability threshold of the instrument, as system gain changes can affect the apparent width of these features. For the measurements in Figure 3, only small gain-changes were necessary. In the north-south direction, depletion regions extend along the entire field of view to include a horizontal distance of more than 1200 km, assuming a 250 km emission height.

The images at 0415 and 0430 UT show the appearance of a second region of airglow depletion drifting into the field of view from the west. This second region seems to be "filled in" before reaching the aircraft. Unstructured airglow (~ 150 to 200 R) covers (most of) the observable sky until 0515 UT and then rapidly falls in intensity (~ 100 R), leaving only minor enhancements towards the southern and western horizons.

3.4 Drifts

The C. G. longitudes of the eastern and western edges of the airglow depletion, on an east-west great circle through the aircraft zenith, were determined for the feature in Figure 3. The results (Figure 4) indicate that the depletion drifted toward C. G. east with a relatively constant velocity of ~ 90 m/sec, while maintaining an east-west dimension of ~ 165 km. Eastward drifts from 50 to 100 m/sec were observed on other local evening flights. During a flight from Lima, Peru, to Homestead AFB, Florida, on 26 March 1977, a clear reversal from eastward to westward drift was observed. This occurred in the midnight (0035 LT) sector with the aircraft located at 16° C. G. latitude. This was the only observation of westward drifts during the expedition.

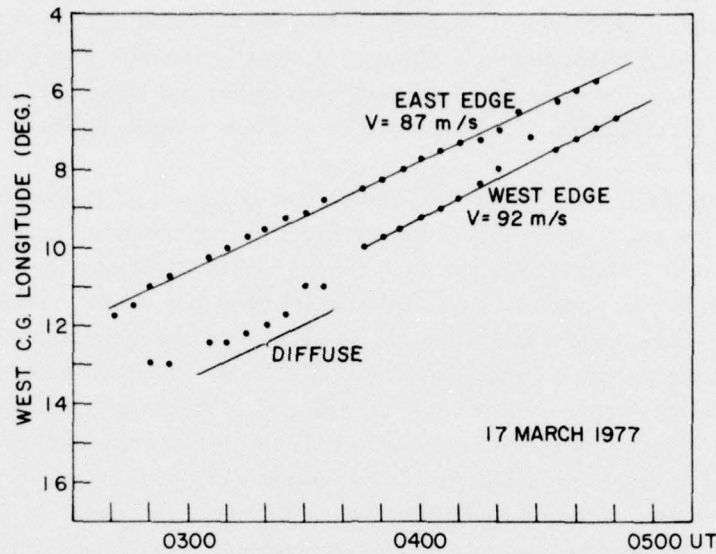


Figure 4. The C.G. Longitude of the Eastern and Western Edges of the Airglow Depletion Shown in Figure 1

3.5 Ionosphere Measurements

Figure 5 presents results of the ionospheric soundings conducted simultaneously with the photometric measurements onboard the aircraft. The virtual height of the observed F-layer and the virtual range of oblique F-layer echoes are shown as a function of time. The oblique echoes are first observed at a virtual range of 800 km at 0157 UT, almost coincident with the initial observation of the airglow depletion on the western horizon. These oblique returns decrease in range, consistent with the approach of a reflecting or scattering region, and merge with the overhead F-layer by 0317 UT.

By 0335 UT, oblique echoes are seen to separate from the lowest F-region trace and increase in range to about 350 km by 0354 UT. After this time they are obscured by other returns and cannot be further identified. Even though the omnidirectional sounder antenna does not permit determination of the angle of arrival of the oblique echoes, the coinciding time histories of the airglow depletion movement and the backscatter range change suggest that the sounder observes the motion of ionospheric scattering regions associated with the motion of the depletion. Assuming a height of 250 km for the scattering region, ranges of the approaching backscatter front were converted to ground distances. The estimated locations of these approaching scattering regions are shown as white dots in the respective

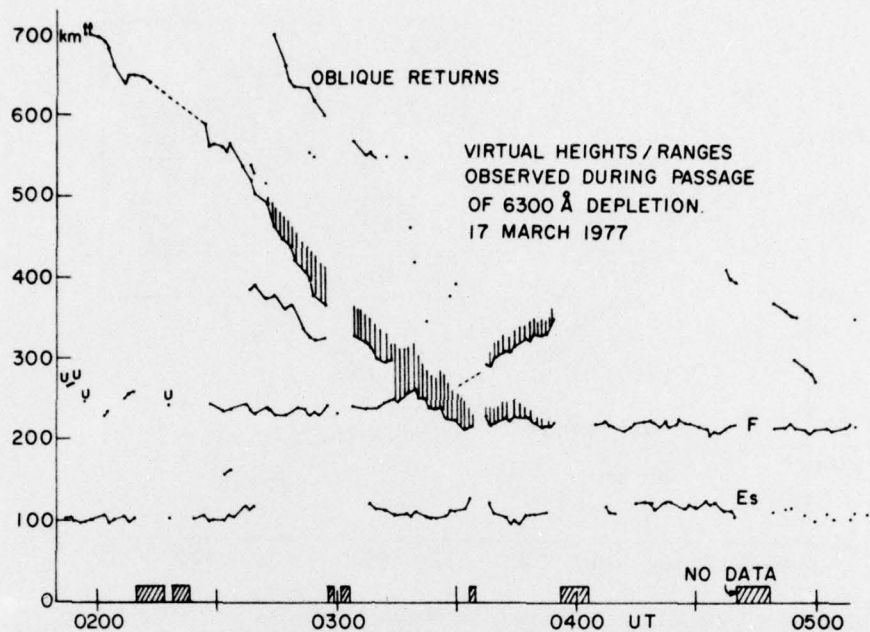


Figure 5. Virtual Height/Range Plot of Ionosonde Returns Associated With the 6300 Å Airglow Depletion. The shaded areas represent range spread on backscatter returns or overhead spread F conditions

airglow images in Figure 3, to the west of zenith. Ground ranges derived from the receding backscatter branch, observed after the overhead passage of the leading edge of the depletion, were entered as black dots to the east of the zenith of the respective images. As Figure 3 shows, best seen in the 0245 to 0315 UT images, the approaching backscatter is tracking the trailing (western) edge of the depletion, while the leading (eastern) edge is tracked by the receding echoes observed after 0330 UT.

A model of an ionization depletion in the bottomside of the ionosphere, shown in Figure 6, produces a sequence of approaching and receding echo traces and a variation in $h'F$, which closely resemble the observations. With the aircraft located to the east of the structure, returns are received vertically and via ray path b1; after passage of the structure to the east of the aircraft, returns are received vertically and via ray path b2. From the all-sky images, the width of the structure has been taken as 165 km and the velocity as 92 m sec^{-1} . The time of passage of the eastern edge through the aircraft zenith was determined as 0308 UT. The virtual heights of the F-layer prior to and after the passage of the

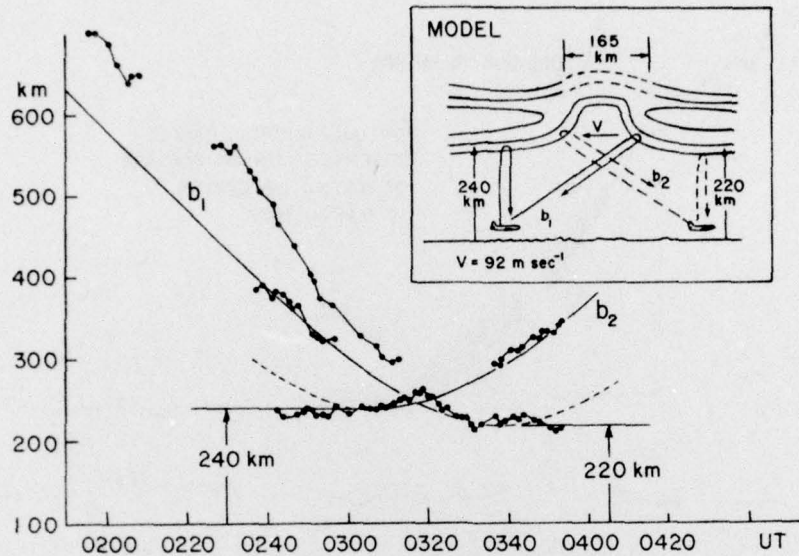


Figure 6. Model of an Eastward Drifting, Bottomside Ne Depletion or Corrugation Based on Observed Ionosonde and Airglow Parameters. The measured ranges of oblique returns and the virtual height of the overhead F-region are compared with range/height changes expected from the passage of the model bottomside structure over the ionosonde

depletion were taken from Figure 3 as 240 km and 220 km respectively. Figure 6 shows the result of the model computations with the relevant sections of the h' plot from Figure 3 superimposed.

The fit is generally good, but additional strong returns associated with the trailing edge of the depletion at ranges larger than those derived from the simple model, and approaching at a greater speed, suggest a more complex structure of the trailing edge than does the model. Analysis of the 16 mm all-sky photometer photographic record, having 30-sec time resolution, shows a distinct structure with turbulent motion at the western edge of the depletion, in contrast to the smooth and stable features observed at the eastern edge. The east-west asymmetry is also visible in Figure 3. The 0330 UT image shows diffuse and patchy structure at the trailing edge compared to the well-defined leading edge. These features may be responsible for the more complex ionosonde backscatter associated with the trailing edge.

The model used to explain the sounder measurements is a simplification of the bottomside effects of an instability model proposed by Woodman and La Hoz⁹ to describe the development and subsequent upward propagation of bubbles of low electron density in the equatorial F-region. This process explains the time history of irregularity structures or plumes observed by the Jicamarca 50 MHz radar. Comparison of the Woodman and La Hoz model with the model shown in Figure 6 suggests that the airglow depletions described here are a manifestation of the same phenomenon leading to the Jicamarca plume observations. Figure 6 also suggests the existence of strong east-west electron density gradients extending over a considerable north-south extent and moving in an eastward direction. These moving fronts are presumably associated with discrete patches of scatterers observed through transequatorial HF propagation experiments.¹⁰ The distinct difference in the structure of the leading and trailing edges of the airglow depletion deduced from the observations of this isolated event may also be responsible for the east-west asymmetry observed in backscatter measurements at 27.8 MHz by Kelleher and Skinner.¹¹

A detailed model of the structure of the F-layer within the airglow depletion cannot be deduced from the available ionograms. The ionogram traces required to establish the Ne (h) profiles are either obscured by the scattered reflections received from the edges of the depletion (see Figure 6) or the traces do not exist due to the irregular structure within the depletion. This limitation of ionosondes to establish profiles within regions of strong horizontal gradients in the high latitude ionosphere is well known; although the main F-layer trough is clearly identifiable in ionograms, the profiles inside the trough cannot be determined due to the narrowness of the depletion.¹²

After the approaching trace merged with the overhead trace, strong unstructured spread F developed and persisted for the period of passage of the depletion. Throughout the evening, the F-layer had come down, initially from 275 km (0000 UT) to 230 km (0300 UT), just prior to the overhead arrival of the leading edge of the depletion. The layer rapidly moved upwards by 35 km, reaching a maximum h' of 265 km by 0319 UT, the time of strongest spread F. After this, the layer again rapidly moved down to 215 km (0332 UT) and fluctuated around

-
9. Woodman, R.F., and La Hoz, C. (1976) Radar observations of F region equatorial irregularities, J. Geophys. Res. 81:5447.
 10. Rottger, J. (1973) Wave-like structures of large scale equatorial spread-F irregularities, J. Atmos. Terr. Phys. 35:1195.
 11. Kelleher, R.F., and Skinner, N.J. (1971) Studies of F-region irregularities at Nairobi, Ann. Geophys. 27:195.
 12. Lobb, R.J., and Titheridge, J.E. (1977) The effect of travelling ionospheric disturbances on ionograms, J. Atmos. Terr. Phys. 39:129.

that level for the remainder of the observations. Some close-range oblique echoes between 0437 UT and 0500 UT are possibly remnants of the ionospheric disturbance associated with the short-lived depletion observed near the western horizon between 0415 UT and 0430 UT.

Observations of foF2 between 0100 and 0500 UT were rather uncertain because of spread conditions and high nighttime HF noise levels, but in general the foF2 fluctuated between 8.5 and 9.5 MHz. After 0500 UT the spread and noise conditions improved and a clear decrease of the f_oF2 from 9.2 MHz (0503 UT) to 8.0 MHz (0532 UT) and finally to 5.8 MHz (0549 UT) was observed, which followed the decrease of the overall brightness of the 0500 UT to 0545 UT all-sky photometer images. Since h'F does not change appreciably (from 212 km at 0503 UT to 226 km at 0549 UT), this change in airglow level is directly attributable to the Ne decay.

3.6 VHF Amplitude Scintillations

During this flight, VHF amplitude measurements were made on the aircraft, using the Lincoln Experimental Satellite (LES-9) 137-MHz down-link transmissions. Fortunately, the direction to the satellite positioned the ray path through the east-west dimension of the airglow depletion, and the eastward drift effectively moved the ray path from lower to higher altitudes through the region. It is important to note that the airglow depletion is a bottomside signature and as such does not reflect characteristics of the topside ionosphere.

Comparison with other types of measurements (Jicamarca Incoherent Radar, aircraft ionosonde, satellite ion and electron density probes) leads to the conclusion that the airglow depletions define the horizontal dimensions of a region of low electron and ion density that extends upward through the F region, often to 1000 km. Ionospheric electron density irregularities with scale sizes from 3 m to 10's of km exist within these depletion regions.

The effect of VHF propagation through the depletion region is shown schematically in Figure 7. A rapid onset of 7 to 14 dB scintillations began at 0400 UT as the ray path reached a height of 275 km within the depletion. Scintillations continued until 0553 UT, which corresponds to an altitude of 800 km.

3.7 Summary of Equatorial Measurements

Monochromatic, all-sky imaging has revealed the existence of north-south (magnetic) aligned regions of airglow depletion in the equatorial F-region. East-west scale sizes of these depletions ranged from 50 to 200 km, with fine structures as small as 2.5 km detectable on the 16 mm photographic records (instrumental resolution at 250 km altitude). Observations during several flights in the immediate vicinity of the magnetic equator in March 1977 show that these depletions drift

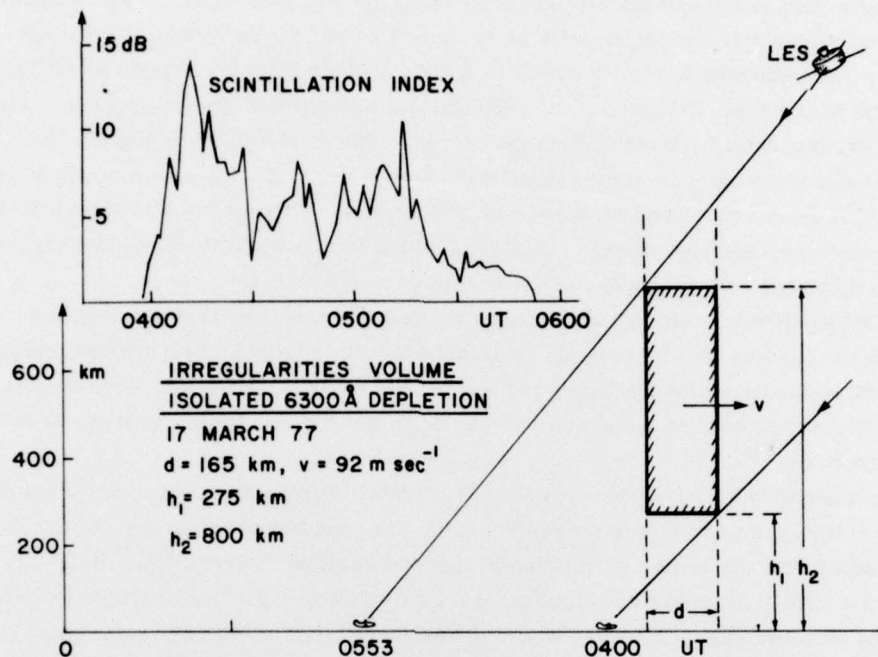


Figure 7. VHF Amplitude Scintillation Index Associated With the Passage of the Ionization Depletion Through the Satellite-to-Aircraft Ray Path

toward the east with speeds of 50 to 100 m/sec during the local evening hours. One example of a reversal from eastward drift velocity to westward drift was observed in the midnight (0035 LT) sector, with the aircraft located at 16° C. G. north. During this expedition, airglow depletions were regularly observed, provided the virtual base height of the adjacent F-layer ($h'F$) was below 275 km. Base heights in excess of 275 km lead to greatly diminished airglow intensities, thus precluding observations of ionospheric irregularities by optical techniques.

A model bottomside Ne depletion — extending for more than 1200 km north-south, 100 to 200 km east-west, and with a base height of the F-layer around 300 km — collocated with the 6300 Å depletion explains both the observed airglow structure and the ionospheric observations. Neither the optical nor the ionosonde techniques could be used to determine the F-layer base height within the region of diminished ionization.

The model is consistent with recent results of McClure et al.¹³ who regularly observed biteouts in the ion density after sunset of up to 3 orders of magnitude with the Atmospheric Explorer satellite AE-C. These biteouts ranged in altitude from the peak of the F-layer up to ~ 600 km and had typical upward plasma velocities of several tens to several hundred m/sec. The model used to explain the sounder observations has strong similarities with the response of the bottomside to a bubble model proposed by Woodman and La Hoz.⁹ From the similarity of the two phenomena, and the models, it is reasonable to postulate that airglow depletions are the optical signatures of these biteouts or bubbles.

Satellite-to-aircraft signal-strength measurements show that propagation through the plasma depletion leads to amplitude scintillation. The altitude range over which scintillation-producing irregularities exist is consistent with plasma bubble measurements of Woodman and La Hoz⁹ and the topside measurement of McClure et al.¹³

Because of the complementary nature of satellite plasma measurements and airborne imaging photometer measurements, coordinated experiments would provide insight into the initial development of these regions of upward plasma flow. Also, the ability of an airborne observatory to monitor a particular region of airglow depletion for several hours would allow successive satellite measurements of ion composition changes during the lifetime of a single bubble.

4. ARCTIC MEASUREMENTS

4.1 Introduction

An expedition was conducted in January 1977 to investigate the effects of low energy particle precipitation into the dayside auroral zone. Because of the low characteristic energy of the precipitating particles, ionization and auroral luminosity are generated at considerably higher altitudes in the dayside zone than in the nightside region. In addition to the study of auroral morphology, this situation provided a unique opportunity to investigate signal fluctuations on VHF/UHF satellite-to-aircraft communications. Propagation through the dayside auroras allows investigation of the effects of F-Region ionization, while propagation through the nightside auroras include both the E- and F-regions.

13. McClure, J. P., Hanson, W. B., and Hoffman, J. F. (1977) Plasma bubbles and irregularities in the equatorial ionosphere, J. Geophys. Res. 82:2650.

4.2 Observations

The flight from Eielson AFB, Alaska, was designed to investigate the noon sector auroras for 5 hr, then return to Eielson along the evening sector of the auroral oval. Figure 8 shows the flight track in corrected geomagnetic (C.G.) coordinates for 21 January 1977. A montage of all-sky images for the entire flight at 10-min intervals is shown in Figures 9a and 9b; they show both the 6300 Å and 4278 Å images oriented with C.G. north at the top of each image and west to the right. A prominent feature is the 6300 Å east-west band visible after 0210 UT. This band is the auroral signature of soft particle precipitation in the dayside cusp region. A notable absence of 4278 Å emission clearly demonstrates the low characteristic energy of the precipitating particles. Unfortunately, instrumental problems prevented measurement of the H_{β} emission; thus, distinction between proton and electron precipitation is not possible. This soft zone extended around to the dusk local time sector (0800 UT), after which a region of more energetic particles was detected.

The structure and dynamics of the 6300 Å emission reflect the spatial and temporal changes that the cusp region exhibits. At 0300 UT the red aurora split into two sections from a previously continuous band. Following this, the morning (western) section drifted equatorward and by 0330 UT the entire region faded below the system intensity threshold (estimated to be 50 R). The 6300 Å emission also displays considerable longitudinal or local time structure, and this structure reflects the spatial variability of the soft particle precipitation region. The image at 0440 UT shows an arc structure that tends to fan out from local noon. This is similar to the structure reported by Snyder and Akasofu¹⁴ and observed by the DMSP satellite auroral images.

At 0810 UT a well-defined auroral arc is visible in both wavelengths. This arc forms the equatorward boundary for particle precipitation and displays the highest average energy of auroras within the field of view. Structured soft particle precipitation is present poleward of the arc.

At 0840 UT, the diffuse or continuous aurora is distinguishable equatorward of the bright arc as a region of unstructured glow at 4278 Å. Although less prominent, this diffuse aurora is also visible at 6300 Å, indicating a broad energy spectrum of the primary beam of precipitating particles. A well-defined substorm began at College at 0940 UT. The change in the aurora from quiet arcs to more active forms after 0940 UT reflects this disturbance.

14. Snyder, A. L., and Akasofu, S. -I. (1976) Auroral oval photographs from the DMSP 8531 and 10533 satellites, *J. Geophys. Res.* 81:1799.

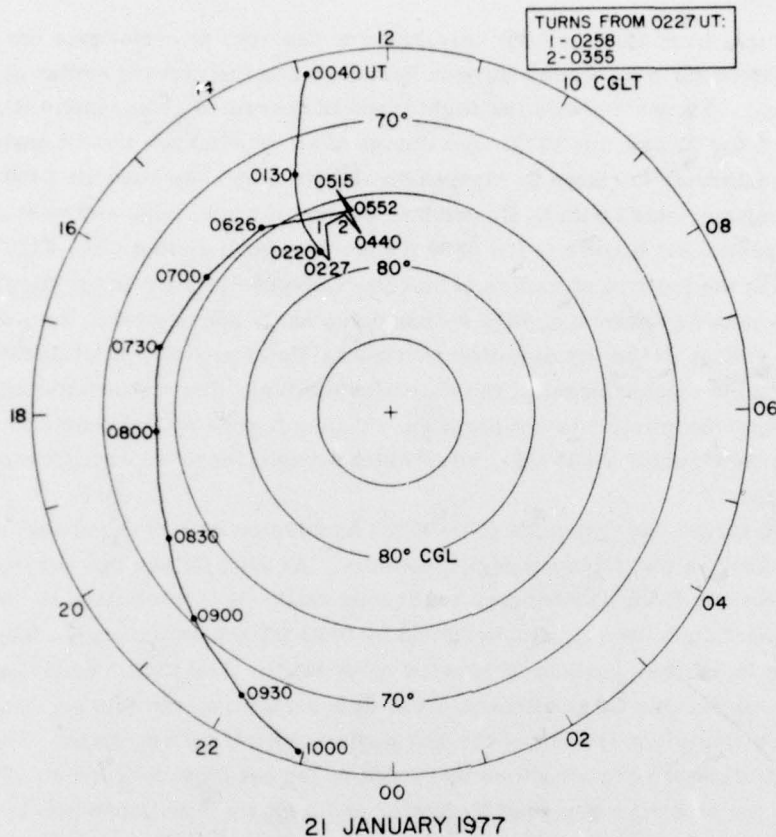


Figure 8. C. G. Latitude/Local Time Plot of the Flight Track of 21 January 1977

During this flight, two orbits of the polar-orbiting DNA WIDEBAND satellite were within the all-sky photometer field of view. This provided an opportunity to investigate the effect of various auroral forms on UHF radio propagation from satellite-to-aircraft. Figure 10 shows the subsatellite track for two orbits, one near local noon and one at late evening. The Universal Time at 1-min intervals is shown along the subsatellite tracks. The field of view of the all-sky photometer, projected to 250 km, is shown for times when the satellite was close to the aircraft. Within the field of view is the 250 km projection of the subsatellite track for each minute, and a schematic representation of the location of the 6300 Å auroras. The actual 6300 Å image, in negative, is also shown. The shaded region along the subsatellite track (and along the 250 km projection) delineates the region where

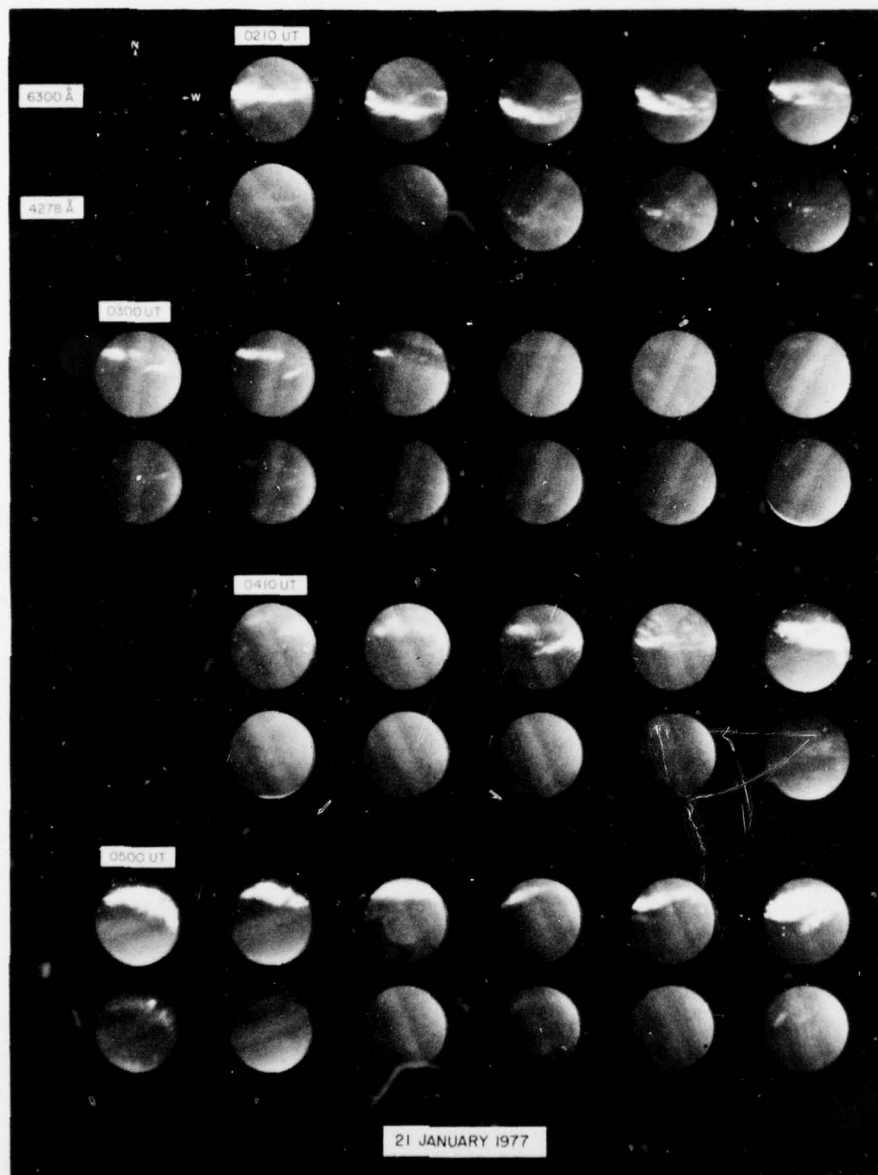


Figure 9a. 6300 Å (top) and 4278 Å (bottom) Images for the Flight of 21 January 1977 From 0210 UT to 0550 UT at 10-Minute Intervals. C.G. north is at the top of each image with west to the right

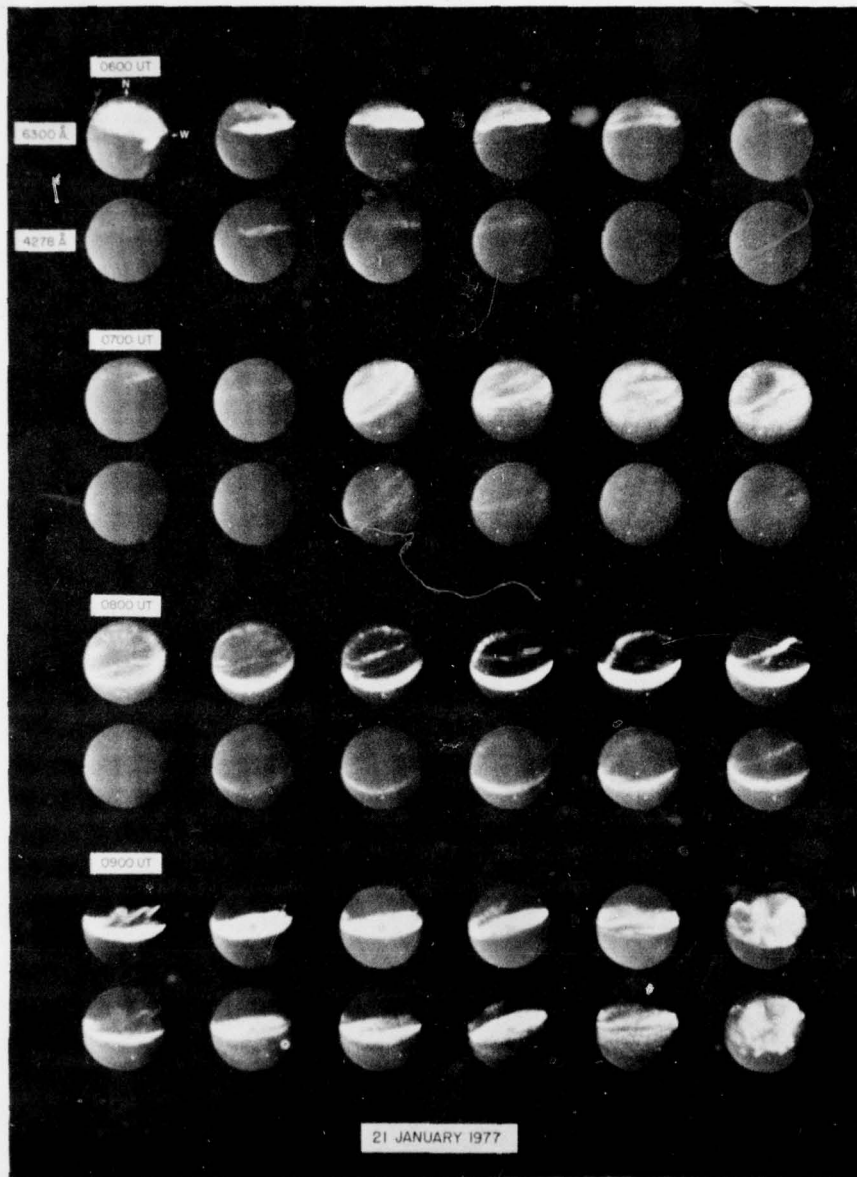


Figure 9b. 6300 Å (top) and 4278 Å (bottom) Images for the Flight of 21 January 1977 From 0600 UT to 0950 UT at 10-Minute Intervals. C.G. north is at the top of each image with west to the right

RELATIONSHIP OF UHF SATCOM SCINTILLATIONS
TO HIGH ALTITUDE AURORAS

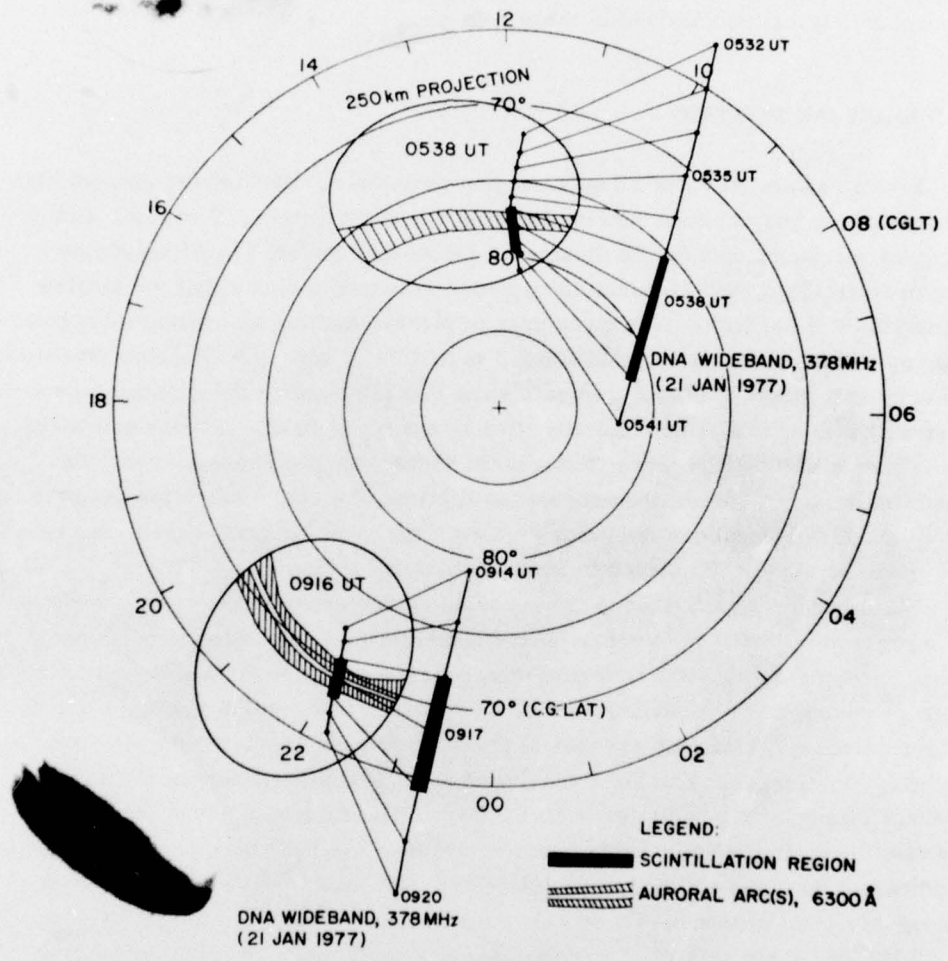


Figure 10. C.G. Latitude/Local Time Plot of Subsatellite Track for Two DNA WIDEBAND Satellite Orbits. Also shown is the simultaneous 6300 Å all-sky photometer image (in negative) and the 250 km projection of the all-sky photometer field of view and the 250 km projection of the subsatellite track. The aurora is shown schematically in the projection

scintillations in excess of 6 dB were encountered. When projected to auroral altitudes, these regions correspond to regions of soft particle precipitation. In the noon sector, the scintillation region extends poleward of the precipitation region. This could be the result of the transport of particle-produced irregularities away from the source region and into the polar cap, according to large scale magnetospheric convection patterns. In other cases, scintillations occur within the boundaries of soft particle precipitation, indicating the presence of F-region ionospheric irregularities within these regions.

5. SUMMARY AND DISCUSSION

Initial results from the all-sky imaging photometer revealed the airglow signatures of ion and electron density depletions in the equatorial F region. Complementary measurements by the Jicamarca Incoherent Radar, the Atmospheric Explorer satellite, and airborne ionospheric sounders indicate that the airglow depletions are the bottomside signatures of plasma bubbles that contain irregularities over the scale size range of from 3 m to 10's of km. Simultaneous transionospheric VHF amplitude measurements show that propagation through these depletion regions cause scintillations that are often in excess of 10 dB. Future equatorial experiments will be directed at three main areas: the post-sunset formation mechanism, temporal changes during the lifetime of a single depletion, and the longitudinal dependence of depletion regions. Airborne, ground-based, and satellite measurements are planned to investigate these areas.

Measurements conducted in the auroral regions provide large scale coverage of auroral precipitation patterns. Monochromatic imaging allows separation of E and F region luminosity, thus providing a semiquantitative determination of the average energy of precipitating particles. The structure and dynamics of the noon sector auroras, which map changes in the dayside cusp precipitation, are visible in the 6300 Å images. The low intensity of the 4278 Å emission reflects the low average energy of the particles in this region. The extension of the soft zone to the dusk local time sector, in the present example, is indicative of quite magnetic conditions. In the evening to midnight sector, auroras of much higher average energy are seen by the increased 4278 Å emission.

UHF amplitude scintillation measurements were made on transionospheric signals through noon and midnight sector auroras. These show similar results, although the E-region ionization profiles differed for the two cases. Ionosonde and optical measurements show virtually no E-region ionization at noon; however, bright 4278 Å auroras and sporadic E ionization (ftEs of 5 to 6 MHz) were present in the nightside region. Since both situations produce similar scintillation effects,

it appears that even weak particle precipitation into the F region is more effective at generating scintillation-producing irregularities than intense precipitation into the E region.

Future measurements in the arctic are planned to investigate the auroral and airglow signatures of the F layer trough and poleward trough wall. Application of large scale optical measurements to trough morphology studies will overcome some problems associated with interpretation of ionosonde measurements in this region.

References

1. Mende, S.B., and Eather, R.H. (1976) Monochromatic all sky observations and auroral precipitation patterns, J. Geophys. Res. 81:3771.
2. Barbier, D. (1961) Les variations d'intensite la raie 6300 Å la luminescence nocturne, Ann. Geophys. 17:5.
3. Barbier, D., Weill, G., and Glaume, J. (1961) L'emission de la raie rouge du ciel nocturne en Afrique, Ann. Geophys. 17:305.
4. Weill, G.M. (1967) Airglow observations near the equator, in Aurora and Airglow, B.M. McCormac, ed., Reinhold Publ. Co., p 407.
5. Kulkarni, P.V. (1974) Tropical airglow, Ann. Geophys. 30:105.
6. Steiger, W.R. (1967) Low latitude observations of airglow, in Aurora and Airglow, B.M. McCormac, ed., Reinhold Publ. Co., p 419.
7. Van Zan, T.E., and Peterson, V.L. (1968) Detailed maps of tropical 6300 Å nightglow enhancements and their implications on the ionospheric F2 layer, Ann. Geophys. 24:747.
8. Mende, S.B., Eather, R.H., and Aamodt, E.K. (1977) Instrument for the monochromatic observation of all sky auroral images, Appl. Opt. 16:1691.
9. Woodman, R.F., and La Hoz, C. (1976) Radar observations of F region equatorial irregularities, J. Geophys. Res. 81:5447.
10. Röttger, J. (1973) Wave-like structures of large scale equatorial spread-F irregularities, J. Atmos. Terr. Phys. 35:1195.
11. Kelleher, R.F., and Skinner, N.J. (1971) Studies of F-region irregularities at Nairobi, Ann. Geophys. 27:195.
12. Lobb, R.J., and Titheridge, J.E. (1977) The effect of travelling ionospheric disturbances on ionograms, J. Atmos. Terr. Phys. 39:129.
13. McClure, J.P., Hanson, W.B., and Hoffman, J.F. (1977) Plasma bubbles and irregularities in the equatorial ionosphere, J. Geophys. Res. 82:2650.
14. Snyder, A.L., and Akasofu, S.-I. (1976) Auroral oval photographs from the DMSP 8531 and 10533 satellites, J. Geophys. Res. 81:1799.